crystals

MDPI

Article

Synthesis of Carbon-Supported MnO_2 Nanocomposites for Supercapacitors Application

Jolita Jablonskiene *, Dijana Simkunaite, Jurate Vaiciuniene, Giedrius Stalnionis, Audrius Drabavicius, Vitalija Jasulaitiene, Vidas Pakstas, Loreta Tamasauskaite-Tamasiunaite * and Eugenijus Norkus

Center for Physical Sciences and Technology, Sauletekio Ave. 3, LT-10257 Vilnius, Lithuania; dijana.simkunaite@ftmc.lt (D.S.); jurate.vaiciuniene@ftmc.lt (J.V.); giedrius.stalnionis@ftmc.lt (G.S.); audrius.drabavicius@ftmc.lt (A.D.); vitalija.jasulaitiene@ftmc.lt (V.J.); vidas.pakstas@ftmc.lt (V.P.); eugenijus.norkus@ftmc.lt (E.N.)

* Correspondence: jolita.jablonskiene@ftmc.lt (J.J.); loreta.tamasauskaite@ftmc.lt (L.T.-T.)

Abstract: In this study, carbon-supported MnO_2 nanocomposites have been prepared using the microwave-assisted heating method followed by two different approaches. The MnO_2/C nanocomposite, labeled as sample S1, was prepared directly by the microwave-assisted synthesis of mixed $KMnO_4$ and carbon powder components. Meanwhile, the other MnO_2/C nanocomposite sample labeled as S2 was prepared indirectly via a two-step procedure that involves the microwave-assisted synthesis of mixed $KMnO_4$ and $MnSO_4$ components to generate MnO_2 and subsequent secondary microwave heating of synthesized MnO_2 species coupled with graphite powder. Field emission scanning electron microscopy (FE-SEM), transmission electron microscopy (TEM), X-ray photoelectron spectroscopy (XPS), and inductively coupled plasma optical emission spectroscopy have been used for characterization of MnO_2/C nanocomposites morphology, structure, and composition. The electrochemical performance of nanocomposites has been investigated using cyclic voltammetry and galvanostatic charge/discharge measurements in a 1 M Na_2SO_4 solution. The MnO_2/C nanocomposite, prepared indirectly via a two-step procedure, displays substantially enhanced electrochemical characteristics. The high specific capacitance of 980.7 F g^{-1} has been achieved from cyclic voltammetry measurements, whereas specific capacitance of 949.3 F g^{-1} at 1 A g^{-1} has been obtained from galvanostatic charge/discharge test for sample S2. In addition, the specific capacitance retention was 93% after 100 cycles at 20 A g^{-1}, indicating good electrochemical stability.

Keywords: supercapacitors; microwave synthesis; nanocomposites; MnO_2

check for updates

Citation: Jablonskiene, J.; Simkunaite, D.; Vaiciuniene, J.; Stalnionis, G.; Drabavicius, A.; Jasulaitiene, V.; Pakstas, V.; Tamasauskaite-Tamasiunaite, L.; Norkus, E. Synthesis of Carbon-Supported MnO_2 Nanocomposites for Supercapacitors Application. *Crystals* **2021**, *11*, 784. https://doi.org/10.3390/cryst11070784

Academic Editor: Fabrizio Pirri

Received: 11 May 2021
Accepted: 1 July 2021
Published: 5 July 2021

1. Introduction

The development of high-performance, environmentally friendly, flexible, light and inexpensive energy storage devices has become one of the most significant worldwide concerns over the past few decades [1–4]. In this regard, supercapacitors (SCs) are widely viewed as potential candidates for next-generation energy storage devices [5,6]. They are of particular interest for high power capability, cyclic stability, safe and simple operation principle, and speedy charge dynamics compared to the other storage devices [7,8].

The decisive role in the fabrication of efficient SCs is directly related to the intrinsic properties of the electrode material used [2,9]. Various new advanced nanostructured materials or their hybrid combinations of two or more components are being looked at. Currently, transition metal oxides (TMOs) coupled mainly with high-surface-area carbon-based materials have been allowed to achieve various hybrid SCs systems, which have superior characteristics of power and energy densities compared to those values obtained at each system separately [10,11]. Among the preferential TMO materials for SCs, a series of manganese oxide-based hybrids were developed recently [12–16]. Exceptional attention has been focused on MnO_2 for its relatively low cost, environmental friendliness, natural abundance, multiple oxidation states of Mn, wide operating voltage range (0–1.00 V vs.

NHE in the neutral electrolyte), and high theoretical specific capacitance (C_s) close to 1370 F g^{-1} [17,18].

However, regardless of the above-mentioned superb characteristics, the main drawback for MnO_2 widespread application is relatively poor electronic (10^{-5}–10^{-6} S cm^{-1}) and ionic (10^{-13} S cm^{-1}) conductivity [8,15]. The experimentally achieved actual capacitance value is far below the theoretically predicted value and depends strongly on the mass loading of MnO_2. Typically it decreases rapidly with the increase in the MnO_2 mass [19]. To improve the capacitive performance of MnO_2, several strategies have been proposed. Nanostructured MnO_2-based electrodes with various morphologies have a high specific surface area and a large surface-to-volume ratio for more effective contact with electrolyte ions, such as mesoporous MnO_2 nanotubes/nanosheets [20], nanowires [21], or flower-like, urchinlike, and nano rodlike structures that have been developed. Multiple-phase heterostructures for high-capacitance electrodes have been created as well [22]. Two high-capacitance crystal phases of MnO_2, namely α-MnO_2 nanowires and δ-MnO_2 ultrathin nanoflakes, have been combined and generated a self-branch heterostructure with a high C_s value of 178 F g^{-1} at 5 mV s^{-1} [22].

To enhance the electric conductivity of MnO_2, the incorporation of conductive metals including Au, Al, Cu, Fe, Mg, Co [23–31] able to act as electron donors have been applied. Changes in electron structure by foreign heteroatoms resulted in the improved capacitive performance of MnO_2 and revealed that, for example, Cu-doped δ -MnO_2 film delivered the maximum C_s value as high as 296 F g^{-1} at 1 A g^{-1} [26]; for Fe-doped MnO_2 nanostructures, this value was of 267.0 F g^{-1} even under a high mass loading of 5 mg cm^{-2} [28]. In the presence of Co, the achieved C_s value was of 350 F g^{-1} at a current density of 0.1 A g^{-1} [29]. The Al-doped MnO_2 demonstrated a high mass and areal specific capacitance of 213 F g^{-1} and 146 F cm^{-2}, respectively, at 0.1 A g^{-1} [25]. Meanwhile, Au-doped MnO_2 showed a high C_s value of 626 F g^{-1} at 5 mV s^{-1} [24].

However, the most effective and currently most widely used way to improve C_s of MnO_2-based electrodes is the deposition of thin films of latter materials on highly conductive and large surface areas containing materials, such as carbon-based substrates, including activated carbon, carbon nanotubes (CNTs), graphene, carbon fiber, or graphitic carbon. Carbon-based materials are the most widely used because of their physical and chemical properties, including low cost, variety of forms, low effort of processing, relatively inert electrochemistry, controllable porosity, and numerous electrocatalytic active sites for a variety of redox reactions [32–34] However, the performance of carbon-based substrates has some limitations related to the insufficient penetration of ions on the inert surface. Therefore, nanohybrids from two or more materials have been developed to overcome such limitations and gained special attention due to synergetic effects in enhancing the surface and electron donor properties. S.V. Prabhakar Vattikuti et al. reported 1D/2Dcarbon-CuO-graphitic carbon nitride (C/CuO@g-C_3N_4) ternary heterostructure that showed a better specific capacitance of 247.2 F g^{-1} compared with the pristine g-C_3N_4 of 83.7 F g^{-1}, at the same time possessing good stability, with 92.1% of the initial capacitance remaining even after 6000 cycles [35]. Newly designed nanohybrids with Bi_2S_3 nanorod core@ amorphous carbon shell heterostructure C@Bi_2S_3 displayed a high specific capacity of 333.43 F g^{-1} at a current density of 1 A g^{-1} and outperformed that of pristine Bi_2S_3 of 124.24 F g^{-1}, due to well-defined cross linkages between the Bi_2S_3 core and carbon shell [36]. The carbon layer was supposed to bind efficiently with Bi_2S_3 nanorods, and thus improve electrical contact with the current collector, confirming the more active carbon participation in the charge/discharge reaction process. These highly porous structures allow the free permeation of electrolyte ensuring rapid movement of ions. Further on, a novel $Na_2Ti_3O_7$/single-walled carbon nanotubes SWCNTs nanostructure electrode material due to high surface area, enriched interfacial conductivity, abundant active edge sites, and mesoporous nature demonstrated a capacity of 576.01 F g^{-1}, at 0.8 A g^{-1}, with cycling stability featuring 91.43% retaining of capacitance after 5000 cycles [37].

Recently, a synergy of such carbon-based materials, featuring excellent conductivity and ultrastability, with MnO_2 substances having less lower conductivity but larger electrochemical capacitance, has allowed overcoming limitations of each material separately by making full use of their advantages due to the synergistic effects between those two types of SCs materials [38–44]. Y. Ping et al. produced the hierarchically porous CJE/MnO_2 composite with a large specific capacitance of 283 F g^{-1} at 1 A g^{-1}, which was on account of high specific surface area (1283 m^2 g^{-1}) and abundant active sites for pseudocapacitance, that particularly resulted from the introduction of MnO_2 [38]. Meanwhile, highly loaded MnOx of 7.02 mg cm^{-2}, electrodeposited on conductive carbon cloth allowed achieving excellent rate capability due to the dual-tuning effect and showed specific capacitance of 161.2 F g^{-1} (1.13 F cm^{-2}) at a high current density of 20 mA cm^{-2} [39]. Recently, an MnO_2 nanowires/graphenated CNTs composite was grown in situ on 316 L stainless steel and exhibited a high capacitance of 495.2 mF cm^{-2} (615.6 F g^{-1}) at a current density of 0.5 mA cm^{-2} and 95% capacity retention after 5000 cycles due to the synergistic effects of the high conductivity of graphenated CNTs and high pseudocapacitance of MnO_2 nanowires [42].

Bearing in mind that the structure of the electrode material directly affects the electrochemical properties of the electrode and simultaneously determines the performance of SCs, different methods have been tested to develop high capacitive MnO_2-based electrode materials. Among them are such methods as hydrothermal synthesis [20,45,46], electrochemical deposition [42,47,48], electrochemical exfoliation [48], electrospinning [49], chemical coprecipitation [50], or even those, using templates [40]. Particular attention has been focused on the simple, fast, cost-effective, and reliable microwave-assisted approach. This method has several advantages that count the possibility to get great gain in energy savings and enhanced fabrication of homogeneous materials since they do not need expensive equipment or complicated procedures; microwave reactions take less time compared to conventional methods and overtake all the substance uniformly, providing uniform particle-size distribution in the sample. Recently, this approach was successfully introduced to synthesize MnO_2 materials that proved themselves for possible use in high-performance supercapacitor applications [51–57].

In this study, the carbon-supported MnO_2 nanocomposites (MnO_2/C) were prepared by the rapid and simple microwave-assisted heating method by employing manganese(II) sulfate ($MnSO_4$) or potassium permanganate ($KMnO_4$) and carbon powder as the microwave absorbing material. The electrochemical properties of the prepared MnO_2/C nanocomposites have been studied to evaluate the possibility of using these nanocomposites as potential supercapacitor electrode materials.

2. Materials and Methods

Graphite powder, $KMnO_4$, $MnSO_4 \cdot H_2O$, Na_2SO_4, polyvinylidene fluoride (2%, PVDF), *N*-methyl-2-pyrrolydone (NMP) were obtained from a Sigma-Aldrich supplier (Taufkirchen, Germany). All reagents were of analytical grade and used as received without further purification. Aqueous solutions were prepared using Milli-Q water with a resistivity of 18.2 MΩ cm^{-1}.

MnO_2/C nanocomposite labeled as sample S1 was prepared by the following steps: 2 g of $KMnO_4$ was mixed with 0.1 g of graphite powder and 20 mL of deionized water in an ultrasound bath for 30 min. Then, the reaction mixture was put into a microwave reactor Monowave 300 (Anton Paar, Graz, Austria). The synthesis of MnO_2/C was carried out at a temperature of 150 °C for 5 min. After that, the precipitate was filtered out, washed with deionized water, and dried in a vacuum oven at a temperature of 80 °C for 2 h. Equation (1) describes the formation of MnO_2 [18]:

$$4KMnO_4 + 3C + H_2O \rightarrow 4MnO_2 + K_2CO_3 + 2KHCO_3 \quad (1)$$

Another MnO_2/C nanocomposite labeled as sample S2 was prepared by the following procedure: at first, the pure MnO_2 was prepared. In a typical experiment, 0.063 g of $KMnO_4$

and 0.1 g of $MnSO_4 \cdot H_2O$ was dispersed in 20 mL of deionized water and mixed in an ultrasound bath for 30 min. Then, the reaction mixture was put into a microwave reactor, and the synthesis was carried out at a temperature of 150 °C for 5 min. The precipitate was filtered out, washed with deionized water, and dried in a vacuum oven at 80 °C for two h. Equation (2) shows the formation process of pure MnO_2 [58]:

$$2KMnO_4 + 3MnSO_4 + 2H_2O \rightarrow 5MnO_2 + 2H_2SO_4 + K_2SO_4 \quad (2)$$

Then, 0.01 g of the prepared MnO_2 was mixed with 0.1 g of graphite powder and 20 mL of deionized water in an ultrasound bath for 30 min. The synthesis of MnO_2/C was carried out under the same conditions as for the sample S1.

The prepared nanocomposites' morphology, structure and composition were characterized using an SEM-focused ion beam facility (Helios Nanolab 650, FEI, Eindhoven, The Netherlands) equipped with an EDX spectrometer (INCA Energy 350 X-Max 20, Oxford Instruments, Oxford, UK). The amount of active material was determined using an ICP optical emission spectrometer Optima700DV (Perkin Elmer, Waltham, MA, USA).

The shape and size of catalyst particles were examined using a Transmission Electron Microscope Tecnai G2 F20 X-TWIN (FEI, Eindhoven, The Netherlands) equipped with an EDAX spectrometer with an r-TEM detector. For microscopic examinations, 10 mg of sample was first sonicated in 1 mL of ethanol for 1 h and then deposited on the Cu grid covered with a continuous carbon film.

XPS measurements were carried out to obtain information about the elemental chemical states and surface composition of powders on the upgraded Vacuum Generator (VG) ESCALAB MKII spectrometer (VG Scientific, UK) fitted with a new XR4 twin anode. The non-monochromatized Al K_α X-ray source was operated at $h\nu$ = 1486.6 eV with 300 W power (20 mA/15 kV), and the pressure in the analysis chamber was lower than 5×10^{-7} Pa during spectral acquisition. The analyzer work function was determined, assuming the binding energy of the Au4f7/2 peak to be 84.0 eV. The spectra were acquired with an electron analyzer pass energy of 20 eV for narrow scans and resolution of 0.05 eV and with a pass energy of 100 eV for survey spectra. All spectra were recorded at a 90° take-off angle. The spectra calibration, processing, and fitting routines were done using Avantage software (v5.962) provided by Thermo VG Scientific (Waltham, MA, USA). Core level peaks of Mn 2p, Mn 3s, O 1s, and C 1s were recorded and analyzed using a nonlinear Shirley-type background. The calculation of the elemental composition was performed on the basis of Scofield's relative sensitivity factors.

XRD patterns of studied powders were measured using an X-ray diffractometer SmartLab (Rigaku, Japan) equipped with a 9 kW rotating Cu anode X-ray tube. The measurements were performed using Bragg–Brentano geometry with a graphite monochromator on the diffracted beam and a step scan mode with the step size of 0.02° (in 2θ scale) and counting time of 1s per step. The measurements were conducted in the 2θ range 10–75°. Phase identification was performed using software package PDXL (Rigaku, Japan) and ICDD powder diffraction database PDF-4+ (2020 release).

All electrochemical measurements were performed with a three-electrode cell using cyclic voltammetry (CV) and galvanostatic charge/discharge (GCD). The prepared MnO_2/C nanocomposites coated on the glassy carbon electrode (GCE) were employed as the working electrode; a Pt sheet as a counter electrode and an Ag/AgCl/KCl electrode were used as a reference. The working electrodes were prepared as follows: the required amount of the active material (MnO_2/C) was dispersed ultrasonically in 2% of PVDF in an NMP solution for 1 h. Then, the obtained slurry was pipetted onto the polished surface of GCE and dried in an oven at a temperature of 80 °C for 2 h.

All electrochemical measurements were performed with a Zennium electrochemical workstation (ZAHNER-Elektrik GmbH & Co.KG, Kronach, Germany). Cyclic voltammograms (CVs) were recorded in a 1 M Na_2SO_4 solution at different scan rates between 10 and 200 mV s^{-1}. All solutions were de-aerated by argon for 15 min before measurements.

The specific capacitance Cs (F g^{-1}) of the electrode material was calculated from the CV test according to the following equation (Equation (3)) [43]:

$$Cs = \frac{1}{m \cdot v \cdot \Delta V} \int idv, \tag{3}$$

where C_s, is the specific capacitance (F g^{-1}), m—the mass of the active material (g), v—the scan rate of potential (V s^{-1}), ΔV—the range of scan potential (V), and i—the current (A).

Further, galvanostatic charge/discharge cycling was carried out within a potential range between 0 and 1 V at a current density of 1, 2, 5, 10, and 20 A g^{-1}. The C_s was calculated using the following equation (Equation (4)) [55]:

$$Cs = \frac{I\Delta t}{m \cdot \Delta V}, \tag{4}$$

where I is the discharge current (A), Δt is the time for a full discharge (s), and ΔV represents the voltage change during the discharge process (V).

3. Results

The carbon-supported MnO_2 nanocomposites were prepared using the microwave-assisted heating method and two different approaches. The MnO_2/C nanocomposite, labeled as sample S1, was prepared directly by the microwave-assisted synthesis of mixed $KMnO_4$ and carbon powder components. Another MnO_2/C nanocomposite, labeled as sample S2, was prepared in another way: at first, pure MnO_2 was obtained by synthesizing $KMnO_4$ and $MnSO_4$. Then, the mixture of the obtained MnO_2 and carbon powder was affected by microwave-assisted heating.

SEM images of the prepared MnO_2/C samples S1 (a, b) and S2 (c, d) under different magnifications are presented in Figure 1.

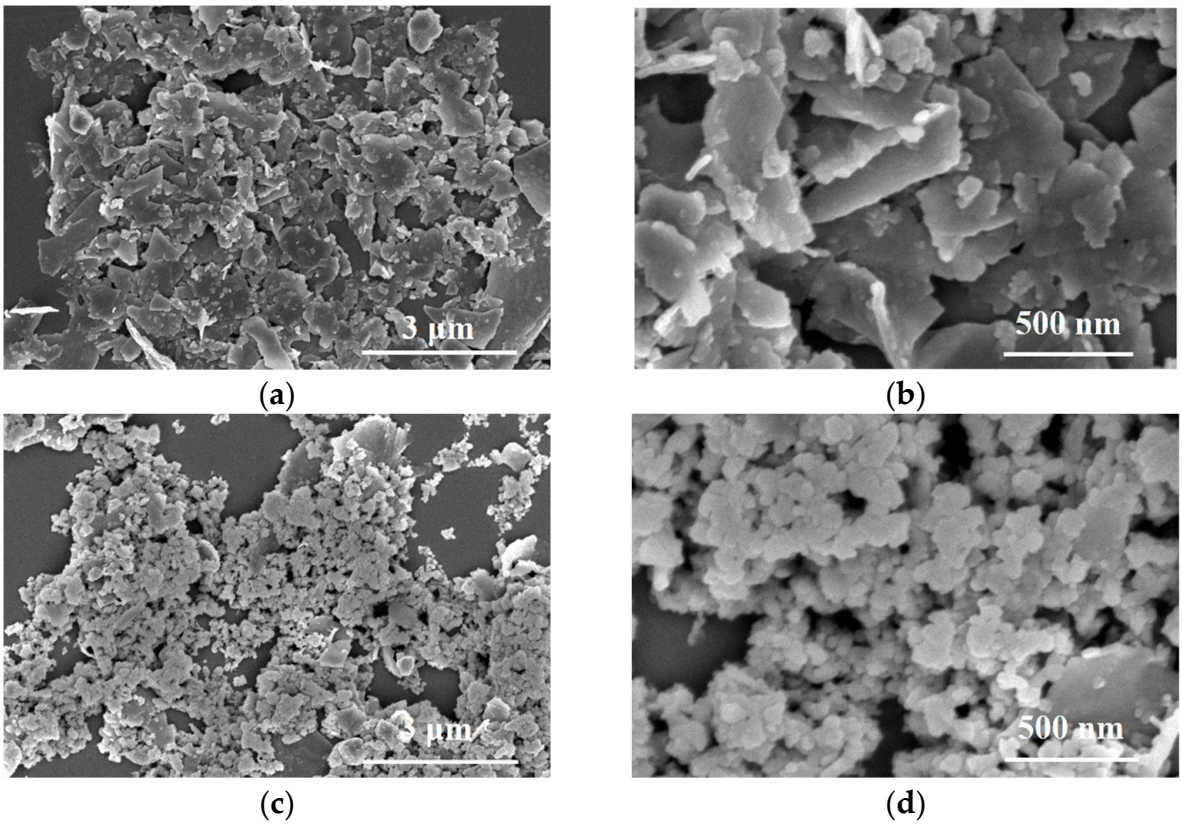

Figure 1. SEM images of MnO_2/C: (**a**,**b**) sample S1; (**c**,**d**) sample S2 under different magnifications.

As evident, both samples are composed of spherical manganese nanograins located on the carbon surface, but they differ significantly in particle number, size and density. In the case of sample S1, a sparse population of almost separate particles under a low MnO_2 aggregation level is arranged (Figure 1a,b). The size of particles in this sample is close to 20 nm. In the case of sample S2, a nanograins' aggregate forms a large porous network structure with carbon embedded inside (Figure 1c,d). The aggregation level of MnO_2 develops to a large extent without any clear interparticle boundaries.

The samples S1 and S2 were further characterized by TEM analysis. TEM images of the samples S1 and S2 confirm the fibrous morphologies of both samples with the more expressed one for sample S2 (Figure 2). It was found that in the prepared sample S1, the MnO_2 nanoparticles are spherical and are ca. 13–18 nm in size (Figure 2a,b). Furthermore, no large MnO_2 nanoparticles are present within the prepared sample, indicating their negligible aggregation. In the case of sample S2, thin flakelike morphology is observed (Figure 2c,d).

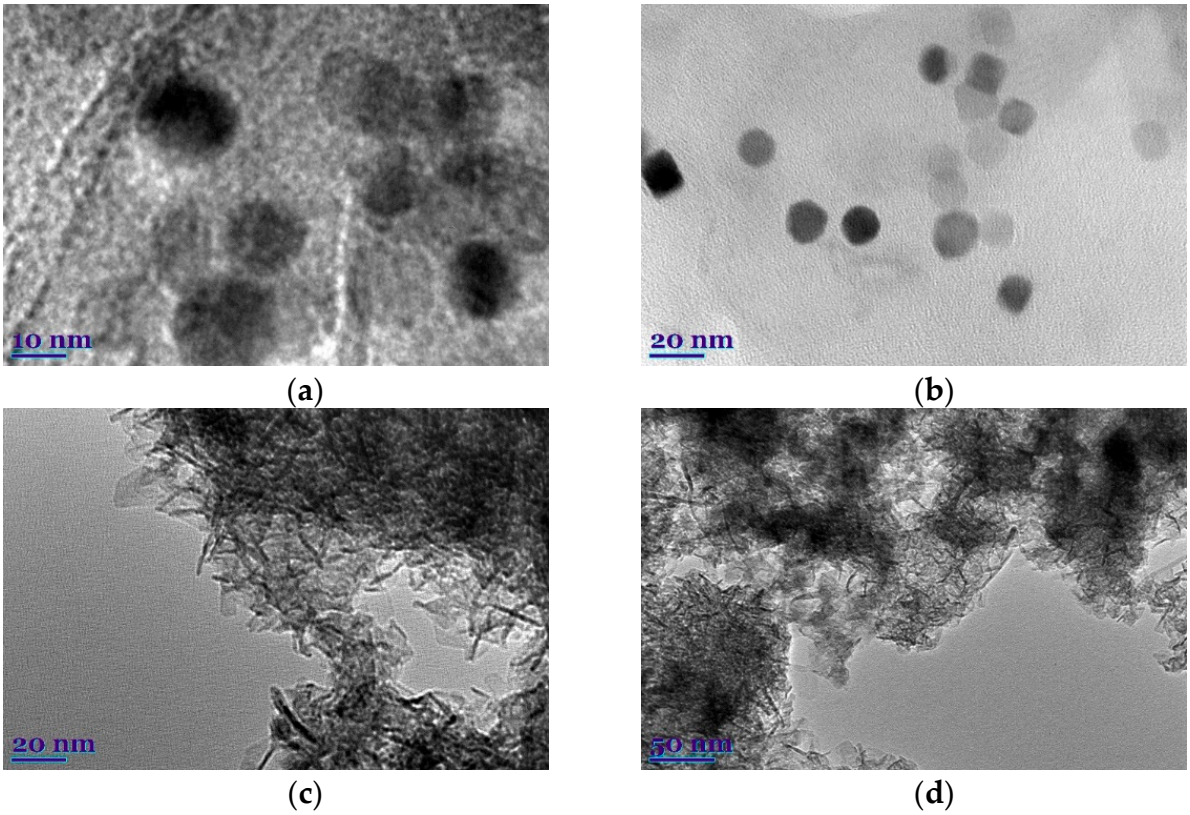

Figure 2. TEM images of MnO_2/C: (**a**,**b**) sample S1; (**c**,**d**) sample S2 under different magnifications.

The chemical composition and the surface electronic state of the prepared MnO_2/C nanocomposites were analyzed using XPS. The C 1s signal and Mn 2p and O 1s peaks were observed in the XPS survey spectra of both samples S1 and S2 (Figure 3a). It indicates the successful synthesis of MnO_2/C, while K content in the samples S1 and S2 was ca. 3.5 and 0.88 at.%, respectively. In both cases, the deconvoluted spectra of Mn show a spin-orbit doublet of the main Mn 2p3/2 and Mn 2p1/2 peaks located at binding energies (E_b) of 642.2 eV and 654.0 eV, respectively, with a spin-energy separation of 11.8 eV (not shown). This value confirms the presence of MnO_2 in the prepared nanocomposites [59–62].

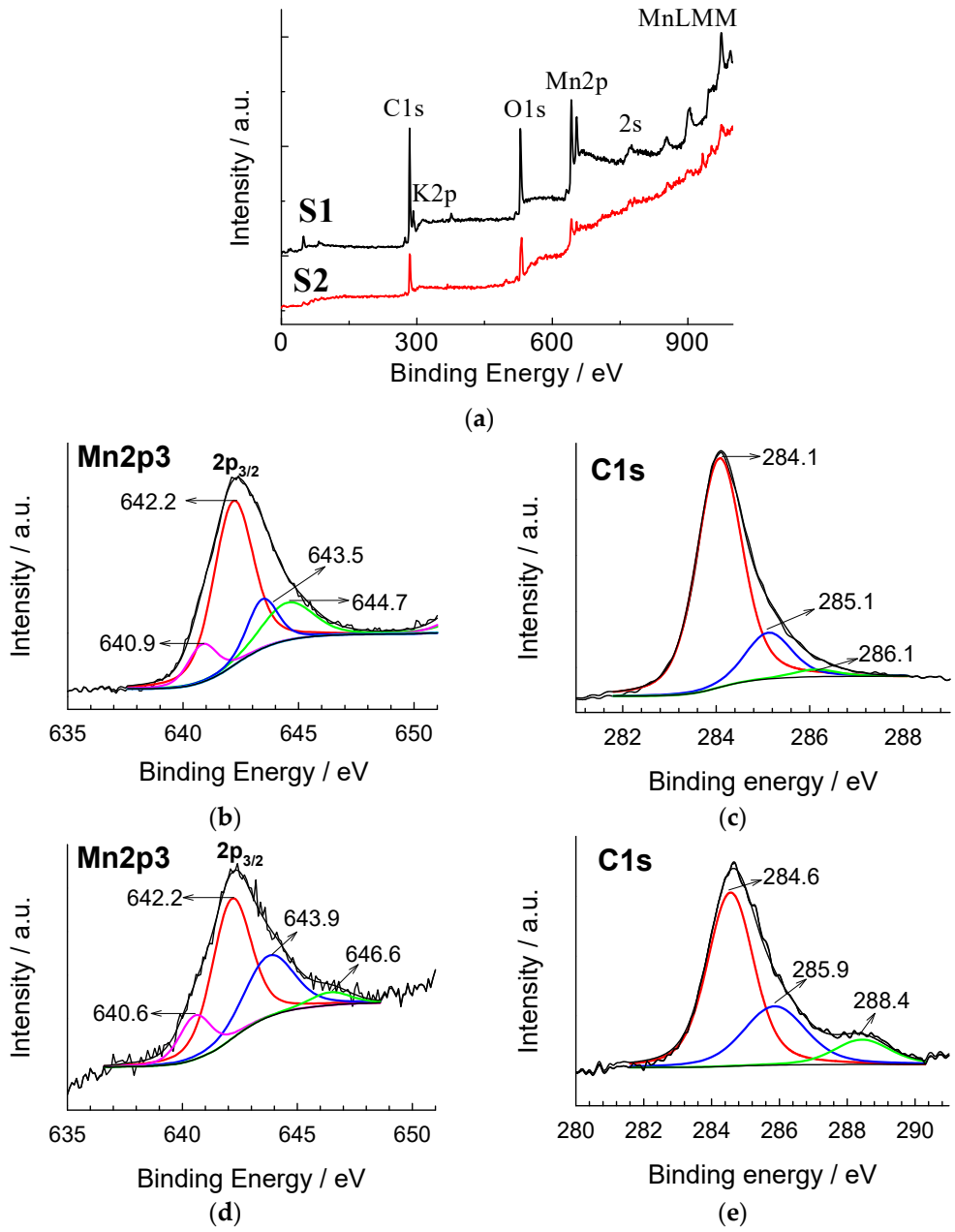

Figure 3. Survey spectra for samples S1 and S2 (**a**). XPS spectra of Mn 2p and C 1s for MnO_2/C: (**b**,**c**) sample S1; (**d**,**e**) sample S2.

XPS spectra of Mn2p3/2 and C 1s for MnO_2/C samples S1 and S2 are shown in Figure 3b–e. As evident, for both samples, the Mn 2p3/2 peaks were deconvoluted into four peaks at binding energies of 640.6 ± 0.3, 642.2, 643.5, and 644.7 and 646.6 eV, indicating the mixed-valence of manganese oxide phases (Figure 3b,c). Following the data reported in [59–64], the position of deconvoluted Mn 2p3/2 peaks are generally assigned to Mn (IV) or Mn (II) oxidation state at E_b ranging between 641.85–643.0 eV or 640.10–641.12 eV, respectively. Therefore, peaks determined at 640.6 ± 0.3 and 642.2 eV confirm the presence of Mn(II) and Mn(IV) species in the samples S1 and S2 (Figure 3b,c). Moreover, the additional peak at 644.7 eV close to that obtained at 644.9 eV in [65,66] could similarly be assigned to a satellite shake-up peak located at higher Eb values than the main component and is a characteristic feature of the MnO phase Mn 2p core peak maximum at 640.6 ± 0.3 eV [67]. Meanwhile, peaks at 643.5 eV and 644.7 eV based on data in [66] could be related to Mn (VI and VII) species in the samples. There is no Mn 2p3/2 signal

(647 eV) from permanganate ions, suggesting permanganate ions have been reduced to MnO_2 [68]. It should be noted that the dominating fraction in the prepared samples S1 and S2 is the MnO_2 phase and is equal to ~59 and 53%, respectively. At the same time, the MnO (Mn (II)) phase remains significantly lower compared to that determined for the MnO_2 (Mn (IV)) phase.

The high-resolution C 1s spectrum for sample S1 can be deconvoluted into three peaks centered at E_b of 284.1, 285.1 and 286.1 eV (Figure 3d). The first one value could be assigned to carbon atoms C–C; meanwhile, other peaks could be assigned to oxygen functionalized carbon atoms, such as C–O, or C–OH and C=O [60,69].

In the case of the sample S2, the C 1s XPS spectrum could be fitted into three peaks at 284.6, 285.8, and 288.4 eV (Figure 3e), which corresponded to C–C/C=C, C–O, and O–C=O bonds, respectively [70]. The strong peak of C–C/C=C bonds shows that carbon contained high graphitization.

The obtained XRD patterns for both MnO_2/C samples are shown in Figure 4. The presence of broad peaks implied that the synthesized samples S1 and S2 are essentially a mixture of amorphous and nanocrystalline phases. The prominent peaks from both samples (Figure 4) locate at 26°, which can be assigned to the (002) crystal plane of graphitic carbon (ICDD card no. 00-056-0159). The diffraction peaks of α-MnO_2 are indexed according to ICDD card no. 04-005-4884, indicating a tetragonal unit cell with lattice parameters of a = b = 9.82 Å and c = 2.85 Å. The synthesized powders are composed of small crystallites with an average size of about 3.2 ± 0.3 nm.

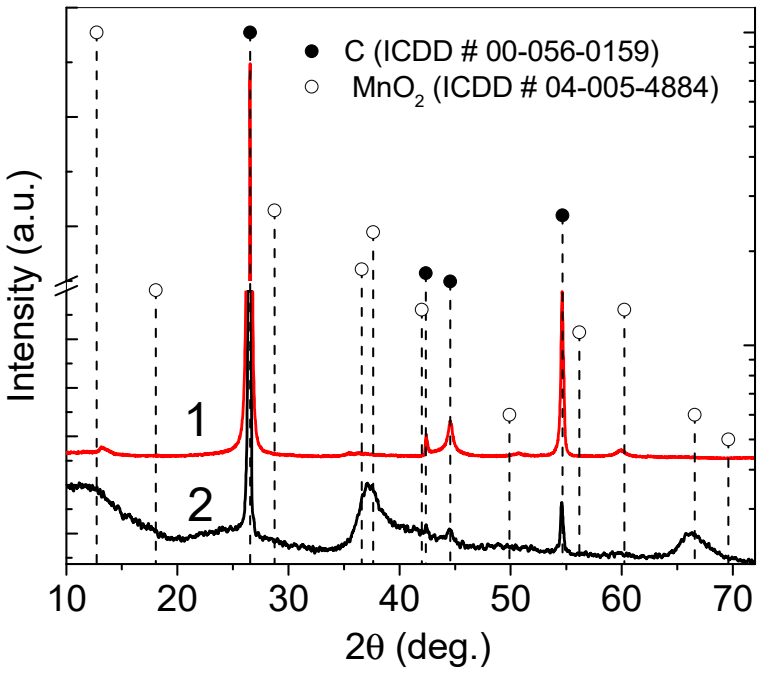

Figure 4. XRD patterns of samples S1 (1 pattern) and sample S2 (2 pattern).

The electrochemical performance of samples S1 and S2 was evaluated from the cyclic voltammetry and galvanostatic charge/discharge measurements using a three-electrode system in a 1 M Na_2SO_4 solution. Figure 5 shows the CV curves of the sample S1 (a), sample S2 (b), and pure carbon (c) at the scan rates of 10, 50, 100, and 200 mV s^{-1}. No obvious peaks are observed in all the CV curves. This indicates that the electrodes are charged and discharge at a constant rate over the complete cycle.

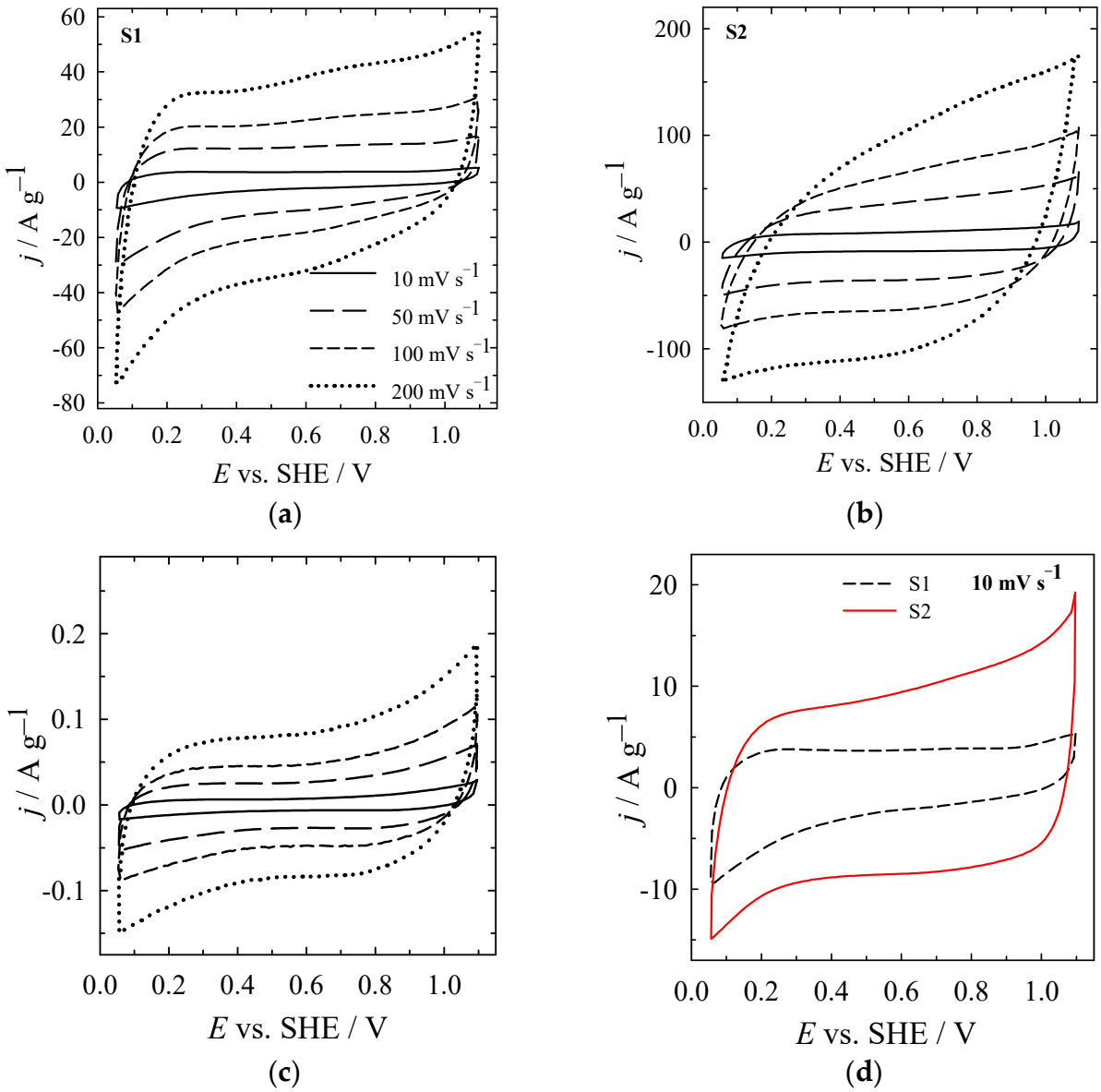

Figure 5. CVs of: (**a**) sample S1; (**b**) sample S2; (**c**) carbon were recorded in 1 M Na_2SO_4 at different scan rates. (**d**) CVs of samples S1 and S2 at 10 mV s^{-1}.

Both sample S1 and carbon show symmetrical rectangular shapes, which indicates the ideal capacitive behavior of those samples (Figure 5a,c). In the case of sample S2, deviations in the rectangularity of CV curves occur (Figure 5b). It can be seen that the current response of sample S2 is significantly higher as compared with that of sample S1 and carbon (Figure 5a–c). It is clearly seen that the sample S2 shows a significantly higher capacitive behavior as compared with that of sample S1 (Figure 5d).

The calculated C_s values for the sample S2 were 980.7, 743.2, 641.0, and 536.6 F g^{-1} at scan rates of 10, 50, 100, and 200 mV s^{-1}, respectively (Figure 6). Meanwhile, for the sample S1, Cs values were 535.8, 349.6, 275.2, and 209.7 F g^{-1} at scan rates of 10, 50, 100, and 200 mV s^{-1}. Those values were found to be ca. 1.8–2.6 times lower than those obtained for sample S2.

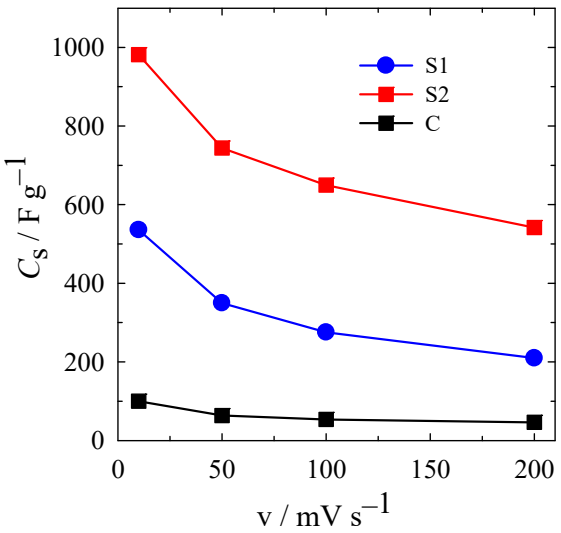

Figure 6. Specific capacitances of the sample S1, sample S2, and carbon obtained from CV curves.

Comparisons of the supercapacitive behavior of various MnO_2-based electrode materials reported in the literature and the present work are listed in Table 1, exhibiting the high specific capacitance of our prepared electrode materials.

Table 1. Comparisons of specific capacitance for various MnO_2-based electrode materials.

Materials	Scan Rate, mV s^{-1}	Specific Capacitance, F g^{-1}	Ref.
MnO_2/C (S2)	10	980.7	This work
MnO_2/C (S1)	10	535.8	This work
Self-branched α-MnO_2/δ-MnO_2 heterojunction nanowires	10	152.0	[22]
MnO_2	5	380.0	[24]
MnO_2	10	154.0	[29]
MnO_2/3D-PC	1	416.0	[47]
MnO_2	5	547.0	[68]
Ultra-long MnO_2 nanowires	2	495.0	[69]
MnO_2 NPs/Ni foam	5	549.0	[71]
MnO_2/MWCNT	2	553.0	[72]

Galvanostatic charge/discharge curves for the sample S2 measured at different current densities of 1, 2, 5, 10, and 20 A g^{-1} are shown in Figure 7a. The shapes of the curves show a typical triangular symmetrical distribution with a slight curvature. This result indicates a combination of electric double-layer and pseudocapacitive contributions. Specific capacitance values were calculated from the discharge test. It was found that the sample S2 can deliver high Cs values of 949.3, 719.3, 480.8, 406.7, and 371.5 F g^{-1} at a current density of 1, 2, 5, 10, and 20 A g^{-1} (Figure 7b). The long-term stability of the charge/discharge process was also performed on this sample S2 at a high current density of 20 A g^{-1} up to 100 cycles (Figure 7c). As evident, this electrode showed excellent long-term stability with 93% retention of its initial capacitance value during 100 cycles.

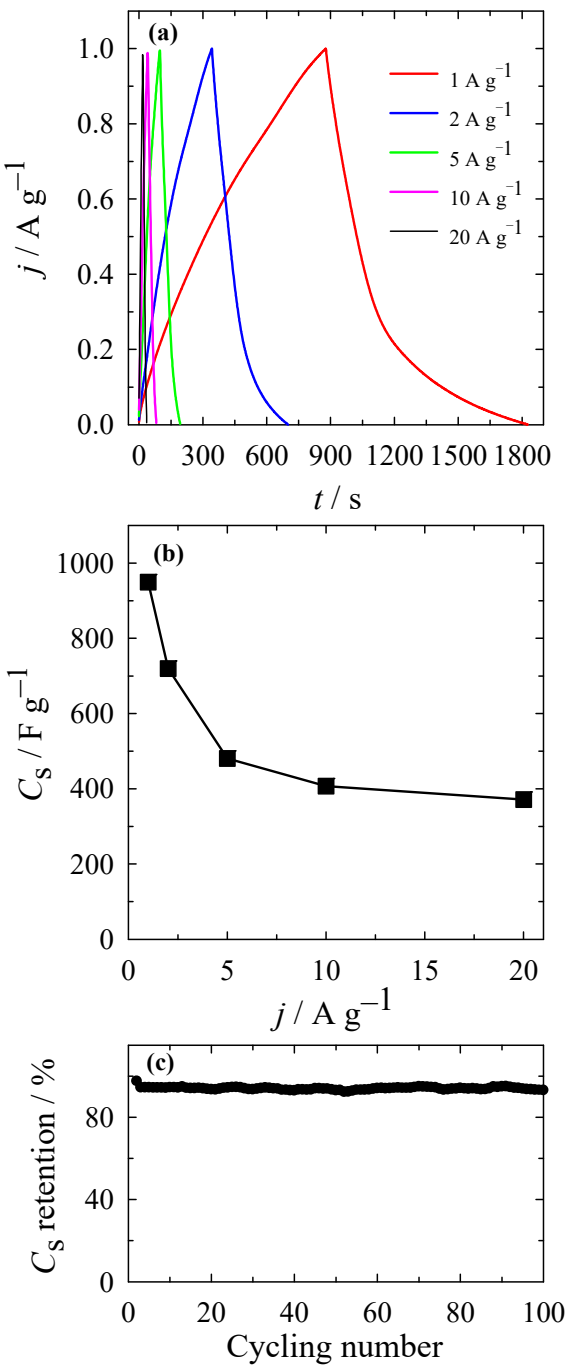

Figure 7. (**a**) Galvanostatic charge/discharge curves of the sample S2 measured at different constant current densities of 1–20 A g^{-1}; (**b**) Specific capacitance obtained from galvanostatic charge/discharge curves with different current densities.

4. Conclusions

We have successfully fabricated carbon-supported MnO_2 nanocomposites via a simple microwave-assisted heating method. Different architecture containing MnO_2 nanocomposites demonstrates improved conductivity, which is a key limitation in pseudocapacitors. The electrochemical measurements revealed that (due to this conductivity) MnO_2/C nanocomposites, especially those prepared via a two-step procedure, exhibit excellent electrochemical performance, including a high specific capacitance of 980.7 F g^{-1}. Moreover, the specific capacitance retention was 93% after 100 cycles at 20 A g^{-1}, indicating good electrochemical stability. The obtained results demonstrate that the prepared MnO_2/C

nanocomposites should be a promising electrode material for supercapacitor applications and could be further extended to fabricate other materials for supercapacitors.

Author Contributions: This study was conducted through the contributions of all authors. Conceptualization, J.J.; L.T.-T. and E.N.; methodology, G.S., A.D., V.P. and V.J.; investigation, J.V., G.S. and A.D.; writing—original draft preparation, J.J. and D.S.; writing—review and editing, L.T.-T. and E.N.; visualization, D.S., J.V., V.P. and V.J. All authors have read and agreed to the published version of the manuscript.

Funding: This research was funded by the European Social Fund under the No 09.3.3-LMT-K-712-02-0142 "Development of Competencies of Scientists, other Researchers, and Students through Practical Research Activities" measure.

Institutional Review Board Statement: Not applicable.

Informed Consent Statement: Not applicable.

Conflicts of Interest: The authors declare no conflict of interest.

References

1. Gopi, C.V.M.; Vinodh, R.; Sambasivam, S.; Obaidat, I.M.; Kim, H.-J. Recent progress of advanced energy storage materials for flexible and wearable supercapacitor: From design and development to applications. *J. Energy Storage* **2020**, *27*, 101035. [CrossRef]
2. Poonam; Sharma, K.; Arora, A.; Tripathi, S.K. Review of supercapacitors: Materials and devices. *J. Energy Storage* **2019**, *21*, 801–825. [CrossRef]
3. Liu, C.; Li, F.; Ma, L.-P.; Cheng, H.-M. Advanced Materials for Energy Storage. *Adv. Mater.* **2010**, *22*, E28–E62. [CrossRef] [PubMed]
4. Miller, E.E.; Hua, Y.; Tezel, F.H. Materials for energy storage: Review of electrode materials and methods of increasing capacitance for supercapacitors. *J. Energy Storage* **2018**, *20*, 30–40. [CrossRef]
5. Wang, F.; Wu, X.; Yuan, X.; Liu, Z.; Zhang, Y.; Fu, L.; Zhu, Y.; Zhou, Q.; Wu, Y.; Huang, W. Latest advances in supercapacitors: From new electrode materials to novel device designs. *Chem. Soc. Rev.* **2017**, *46*, 6816–6854. [CrossRef] [PubMed]
6. Liu, C.; Yan, X.; Hu, F.; Gao, G.; Wu, G.; Yang, X. Toward Superior Capacitive Energy Storage: Recent Advances in Pore Engineering for Dense Electrodes. *Adv. Mater.* **2018**, *30*, e1705713. [CrossRef] [PubMed]
7. Simon, P.; Gogotsi, Y. Materials for electrochemical capacitors. *Nat. Mater.* **2008**, *7*, 845–854. [CrossRef]
8. Guo, W.; Yu, C.; Li, S.; Wang, Z.; Yu, J.; Huang, H.; Qiu, J. Strategies and insights towards the intrinsic capacitive properties of MnO_2 for supercapacitors: Challenges and perspectives. *Nano Energy* **2019**, *57*, 459–472. [CrossRef]
9. Wang, G.; Zhang, L.; Zhang, J. A review of electrode materials for electrochemical supercapacitors. *Chem. Soc. Rev.* **2012**, *41*, 797–828. [CrossRef]
10. Muzaffar, A.; Ahamed, M.B.; Deshmukh, K.; Thirumalai, J. A review on recent advances in hybrid supercapacitors: Design, fabrication and applications. *Renew. Sustain. Energy Rev.* **2019**, *101*, 123–145. [CrossRef]
11. Afif, A.; Rahman, S.M.; Azad, A.T.; Zaini, J.; Islam, A.; Azad, A. Advanced materials and technologies for hybrid supercapacitors for energy storage—A review. *J. Energy Storage* **2019**, *25*, 100852. [CrossRef]
12. Xu, W.; Jiang, Z.; Yang, Q.; Huo, W.; Javed, M.S.; Li, Y.; Huang, L.; Gu, X.; Hu, C. Approaching the lithium-manganese oxides' energy storage limit with Li_2MnO_3 nanorods for high-performance supercapacitor. *Nano Energy* **2018**, *43*, 168–176. [CrossRef]
13. Xia, H.; Hong, C.; Li, B.; Zhao, B.; Lin, Z.; Zheng, M.; Savilov, S.V.; Aldoshin, S.M. Facile Synthesis of Hematite Quantum-Dot/Functionalized Graphene-Sheet Composites as Advanced Anode Materials for Asymmetric Supercapacitors. *Adv. Funct. Mater.* **2015**, *25*, 627–635. [CrossRef]
14. Qiu, T.; Luo, B.; Giersig, M.; Akinoglu, E.M.; Hao, L.; Wang, X.; Shi, L.; Jin, M.; Zhi, L. Au@MnO_2 Core-Shell Nanomesh Electrodes for Transparent Flexible Supercapacitors. *Small* **2014**, *10*, 4136–4141. [CrossRef]
15. Huang, M.; Zhang, Y.; Li, F.; Zhang, L.; Wen, Z.; Liu, Q. Facile synthesis of hierarchical Co_3O_4@MnO_2 core–shell arrays on Ni foam for asymmetric supercapacitors. *J. Power Sources* **2014**, *252*, 98–106. [CrossRef]
16. Radhamani, A.V.; Shareef, K.M.; Rao, M.S.R. ZnO@MnO_2 Core–Shell Nanofiber Cathodes for High Performance Asymmetric Supercapacitors. *ACS Appl. Mater. Interfaces* **2016**, *8*, 30531–30542. [CrossRef]
17. Wang, Y.; Zeng, J.; Li, J.; Cui, X.; Al-Enizi, A.M.; Zhang, L.; Zheng, G. One-dimensional nanostructures for flexible supercapacitors. *J. Mater. Chem. A* **2015**, *3*, 16382–16392. [CrossRef]
18. Liu, L.; Niu, Z.; Chen, J. Unconventional supercapacitors from nanocarbon-based electrode materials to device configurations. *Chem. Soc. Rev.* **2016**, *45*, 4340–4363. [CrossRef]
19. Huang, M.; Li, F.; Dong, F.; Zhang, Y.X.; Zhang, L. MnO_2-based nanostructures for high-performance supercapacitors. *J. Mater. Chem. A* **2015**, *3*, 21380–21423. [CrossRef]
20. Huang, M.; Zhang, Y.; Li, F.; Zhang, L.; Ruoff, R.S.; Wen, Z.; Liu, Q. Self-Assembly of Mesoporous Nanotubes Assembled from Interwoven Ultrathin Birnessite-type MnO_2 Nanosheets for Asymmetric Supercapacitors. *Sci. Rep.* **2015**, *4*, 3878. [CrossRef]

21. Yin, B.; Zhang, S.; Jiao, Y.; Liu, Y.; Qu, F.; Wu, X. Facile synthesis of ultralong MnO_2 nanowires as high performance supercapacitor electrodes and photocatalysts with enhanced photocatalytic activities. *CrystEngComm* **2014**, *16*, 9999–10005. [CrossRef]
22. Zhu, C.; Yang, L.; Seo, J.K.; Zhang, X.; Wang, S.; Shin, J.; Chao, D.; Zhang, H.; Meng, Y.S.; Fan, H.J. Self-branched α-MnO_2/δ-MnO_2 heterojunction nanowires with enhanced pseudocapacitance. *Mater. Horiz.* **2017**, *4*, 415–422. [CrossRef]
23. Lv, Q.; Sun, H.; Li, X.; Xiao, J.; Xiao, F.; Liu, L.; Luo, J.; Wang, S. Ultrahigh capacitive performance of three-dimensional electrode nanomaterials based on α-MnO_2 nanocrystallines induced by doping Au through Å-scale channels. *Nano Energy* **2016**, *21*, 39–50. [CrossRef]
24. Kang, J.; Hirata, A.; Kang, L.; Zhang, X.; Hou, Y.; Chen, L.; Li, C.; Fujita, T.; Akagi, K.; Chen, M. Enhanced Supercapacitor Performance of MnO_2 by Atomic Doping. *Angew. Chem. Int. Ed.* **2013**, *52*, 1664–1667. [CrossRef] [PubMed]
25. Hu, Z.; Xiao, X.; Chen, C.; Li, T.; Huang, L.; Zhang, C.; Su, J.; Miao, L.; Jiang, J.; Zhang, Y.; et al. Al-doped α-MnO_2 for high mass-loading pseudocapacitor with excellent cycling stability. *Nano Energy* **2015**, *11*, 226–234. [CrossRef]
26. Su, X.; Yu, L.; Cheng, G.; Zhang, H.; Sun, M.; Zhang, L.; Zhang, J. Controllable hydrothermal synthesis of Cu-doped δ-MnO_2 films with different morphologies for energy storage and conversion using supercapacitors. *Appl. Energy* **2014**, *134*, 439–445. [CrossRef]
27. Peng, R.; Wu, N.; Zheng, Y.; Huang, Y.; Luo, Y.; Yu, P.; Zhuang, L. Large-Scale Synthesis of Metal-Ion-Doped Manganese Dioxide for Enhanced Electrochemical Performance. *ACS Appl. Mater. Interfaces* **2016**, *8*, 8474–8480. [CrossRef]
28. Wang, Z.; Wang, F.; Li, Y.; Hu, J.; Lu, Y.; Xu, M. Interlinked multiphase Fe-doped MnO_2 nanostructures: A novel design for enhanced pseudocapacitive performance. *Nanoscale* **2016**, *8*, 7309–7317. [CrossRef]
29. Tang, C.-L.; Wei, X.; Jiang, Y.-M.; Wu, X.-Y.; Wang, K.-X.; Chen, J.-S.; Han, L.-N. Cobalt-Doped MnO_2 Hierarchical Yolk–Shell Spheres with Improved Supercapacitive Performance. *J. Phys. Chem. C* **2015**, *119*, 8465–8471. [CrossRef]
30. Hashem, A.M.A.; Abuzeid, H.M.; Narayanan, N.; Ehrenberg, H.; Julien, C. Synthesis, structure, magnetic, electrical and electrochemical properties of Al, Cu and Mg doped MnO_2. *Mater. Chem. Phys.* **2011**, *130*, 33–38. [CrossRef]
31. Zhang, X.; Meng, X.; Gong, S.; Li, P.; Jin, L.; Cao, Q. Synthesis and characterization of 3D MnO_2/carbon microtube bundle for supercapacitor electrodes. *Mater. Lett.* **2016**, *179*, 73–77. [CrossRef]
32. Pandolfo, A.; Hollenkamp, A. Carbon properties and their role in supercapacitors. *J. Power Sources* **2006**, *157*, 11–27. [CrossRef]
33. Frackowiak, E. Carbon materials for supercapacitor application. *Phys. Chem. Chem. Phys.* **2007**, *9*, 1774–1785. [CrossRef] [PubMed]
34. Zhang, L.; Zhao, X.S. Carbon-based materials as supercapacitor electrodes. *Chem. Soc. Rev.* **2009**, *38*, 2520–2531. [CrossRef] [PubMed]
35. Vattikuti, S.P.; Reddy, B.P.; Byon, C.; Shim, J. Carbon/CuO nanosphere-anchored g-C_3N_4 nanosheets as ternary electrode material for supercapacitors. *J. Solid State Chem.* **2018**, *262*, 106–111. [CrossRef]
36. Vattikuti, S.V.P.; Police, A.K.R.; Shim, J.; Byon, C. Sacrificial-template-free synthesis of core-shell C@Bi_2S_3 heterostructures for efficient supercapacitor and H_2 production applications. *Sci. Rep.* **2018**, *8*, 4194. [CrossRef]
37. Vattikuti, S.P.; Devarayapalli, K.C.; Dang, N.N.; Shim, J. 1D/1D $Na_2Ti_3O_7$/SWCNTs electrode for split-cell-type asymmetric supercapacitor device. *Ceram. Int.* **2021**, *47*, 11602–11610. [CrossRef]
38. Ping, Y.; Liu, Z.; Li, J.; Han, J.; Yang, Y.; Xiong, B.; Fang, P.; He, C. Boosting the performance of supercapacitors based hierarchically porous carbon from natural Juncus effuses by incorporation of MnO_2. *J. Alloys Compd.* **2019**, *805*, 822–830. [CrossRef]
39. Feng, D.-Y.; Sun, Z.; Huang, Z.-H.; Cai, X.; Song, Y.; Liu, X.-X. Highly loaded manganese oxide with high rate capability for capacitive applications. *J. Power Sources* **2018**, *396*, 238–245. [CrossRef]
40. Sun, L.; Li, N.; Zhang, S.; Yu, X.; Liu, C.; Zhou, Y.; Han, S.; Wang, W.; Wang, Z. Nitrogen-containing porous carbon/α-MnO_2 nanowires composite electrode towards supercapacitor applications. *J. Alloys Compd.* **2019**, *789*, 910–918. [CrossRef]
41. Su, X.; Yu, L.; Cheng, G.; Zhang, H.; Sun, M.; Zhang, X. High-performance α-MnO_2 nanowire electrode for supercapacitors. *Appl. Energy* **2015**, *153*, 94–100. [CrossRef]
42. Lei, R.; Zhang, H.; Lei, W.; Li, D.; Fang, Q.; Ni, H.; Gu, H. MnO_2 nanowires electrodeposited on freestanding graphenated carbon nanotubes as binder-free electrodes with enhanced supercapacitor performance. *Mater. Lett.* **2019**, *249*, 140–142. [CrossRef]
43. Meng, X.; Lu, L.; Sun, C. Green Synthesis of Three-Dimensional MnO_2/Graphene Hydrogel Composites as a High-Performance Electrode Material for Supercapacitors. *ACS Appl. Mater. Interfaces* **2018**, *10*, 16474–16481. [CrossRef] [PubMed]
44. Qiu, Y.; Xu, P.; Guo, B.; Cheng, Z.; Fan, H.; Yang, M.; Yang, X.; Li, J. Electrodeposition of manganese dioxide film on activated carbon paper and its application in supercapacitors with high rate capability. *RSC Adv.* **2014**, *4*, 64187–64192. [CrossRef]
45. Cheng, H.; Zhao, S.; Yi, F.; Gao, A.; Shu, D.; Ao, Z.; Huang, S.; Zhou, X.; He, C.; Li, S.; et al. Supramolecule-assisted synthesis of in-situ carbon-coated MnO_2 nanosphere for supercapacitors. *J. Alloys Compd.* **2019**, *779*, 550–556. [CrossRef]
46. Yang, M.; Kim, D.S.; Hong, S.B.; Sim, J.-W.; Kim, J.; Kim, S.-S.; Choi, B.G. MnO_2 Nanowire/Biomass-Derived Carbon from Hemp Stem for High-Performance Supercapacitors. *Langmuir* **2017**, *33*, 5140–5147. [CrossRef]
47. Wang, L.; Zheng, Y.; Chen, S.; Ye, Y.; Xu, F.; Tan, H.; Li, Z.; Hou, H.; Song, Y. Three-Dimensional Kenaf Stem-Derived Porous Carbon/MnO_2 for High-Performance Supercapacitors. *Electrochim. Acta* **2014**, *135*, 380–387. [CrossRef]
48. Wang, H.; Fu, Q.; Pan, C. Green mass synthesis of graphene oxide and its MnO_2 composite for high performance supercapacitor. *Electrochim. Acta* **2019**, *312*, 11–21. [CrossRef]
49. Nie, G.; Lu, X.; Chi, M.; Gao, M.; Wang, C. General synthesis of hierarchical C/MOx@MnO_2 (M = Mn, Cu, Co) composite nanofibers for high-performance supercapacitor electrodes. *J. Colloid Interface Sci.* **2018**, *509*, 235–244. [CrossRef]

50. Wang, X.; Chen, S.; Li, D.; Sun, S.; Peng, Z.; Komarneni, S.; Yang, D. Direct Interfacial Growth of MnO_2 Nanostructure on Hierarchically Porous Carbon for High-Performance Asymmetric Supercapacitors. *ACS Sustain. Chem. Eng.* **2018**, *6*, 633–641. [CrossRef]
51. Kang, H.G.; Jeong, J.; Hong, S.B.; Lee, G.Y.; Kim, D.H.; Kim, J.W.; Choi, B.G. Scalable exfoliation and activation of graphite into porous graphene using microwaves for high–performance supercapacitors. *J. Alloys Compd.* **2019**, *770*, 458–465. [CrossRef]
52. Bi, Y.; Nautiyal, A.; Zhang, H.; Yan, H.; Luo, J.; Zhang, X. Facile and ultrafast solid-state microwave approach to MnO_2-NW@Graphite nanocomposites for supercapacitors. *Ceram. Int.* **2018**, *44*, 5402–5410. [CrossRef]
53. Wang, F.; Zhou, Q.; Li, G.; Wang, Q. Microwave preparation of 3D flower-like $MnO_2/Ni(OH)_2$/nickel foam composite for high-performance supercapacitors. *J. Alloys Compd.* **2017**, *700*, 185–190. [CrossRef]
54. Zhang, X.; Miao, W.; Li, C.; Sun, X.; Wang, K.; Ma, Y. Microwave-assisted rapid synthesis of birnessite-type MnO_2 nanoparticles for high performance supercapacitor applications. *Mater. Res. Bull.* **2015**, *71*, 111–115. [CrossRef]
55. Zhang, X.; Sun, X.; Zhang, H.; Zhang, D.; Ma, Y. Microwave-assisted reflux rapid synthesis of MnO_2 nanostructures and their application in supercapacitors. *Electrochim. Acta* **2013**, *87*, 637–644. [CrossRef]
56. Meher, S.K.; Rao, G.R. Enhanced activity of microwave synthesized hierarchical MnO_2 for high performance supercapacitor applications. *J. Power Sources* **2012**, *215*, 317–328. [CrossRef]
57. Li, Y.; Wang, J.; Zhang, Y.; Banis, M.N.; Liu, J.; Geng, D.; Li, R.; Sun, X. Facile controlled synthesis and growth mechanisms of flower-like and tubular MnO_2 nanostructures by microwave-assisted hydrothermal method. *J. Colloid Interface Sci.* **2012**, *369*, 123–128. [CrossRef]
58. Bagotsky, V.S.; Skundin, A.M.; Volfkovich, Y.M. *Electrochemical Power Sources—Batteries, Fuel Cells, and Supercapacitors*; John Wiley & Sons: Hoboken, NJ, USA, 2015.
59. Audi, A.A.; Sherwood, P. Valence-band X-ray photoelectron spectroscopic studies of manganese and its oxides interpreted by cluster and band structure calculations. *Surf. Interface Anal.* **2002**, *33*, 274–282. [CrossRef]
60. Zhou, D.; Lin, H.; Zhang, F.; Niu, H.; Cui, L.; Wang, Q.; Qu, F. Freestanding MnO_2 nanoflakes/porous carbon nanofibers for high-performance flexible supercapacitor electrodes. *Electrochim. Acta* **2015**, *161*, 427–435. [CrossRef]
61. Ramírez, A.; Hillebrand, P.; Stellmach, D.; May, M.; Bogdanoff, P.; Fiechter, S. Evaluation of MnOx, Mn_2O_3, and Mn_3O_4 Electrodeposited Films for the Oxygen Evolution Reaction of Water. *J. Phys. Chem. C* **2014**, *118*, 14073–14081. [CrossRef]
62. NIST X-ray Photoelectron Spectroscopy Database. Available online: https://srdata.nist.gov/xps/ (accessed on 11 May 2021).
63. Ilton, E.S.; Post, J.E.; Heaney, P.J.; Ling, F.T.; Kerisit, S.N. XPS determination of Mn oxidation states in Mn (hydr)oxides. *Appl. Surf. Sci.* **2016**, *366*, 475–485. [CrossRef]
64. Baer, D.R.; Artyushkova, K.; Cohen, H.; Easton, C.D.; Engelhard, M.; Gengenbach, T.R.; Greczynski, G.; Mack, P.; Morgan, D.J.; Roberts, A. XPS guide: Charge neutralization and binding energy referencing for insulating samples. *J. Vac. Sci. Technol. A* **2020**, *38*, 031204. [CrossRef]
65. Beyazay, T.; Oztuna, F.E.S.; Unal, U. Self-Standing Reduced Graphene Oxide Papers Electrodeposited with Manganese Oxide Nanostructures as Electrodes for Electrochemical Capacitors. *Electrochim. Acta* **2019**, *296*, 916–924. [CrossRef]
66. Biesinger, M.C.; Payne, B.P.; Grosvenor, A.P.; Lau, L.W.; Gerson, A.R.; Smart, R.S. Resolving surface chemical states in XPS analysis of first row transition metals, oxides and hydroxides: Cr, Mn, Fe, Co and Ni. *Appl. Surf. Sci.* **2011**, *257*, 2717–2730. [CrossRef]
67. Grissa, R.; Martinez, H.; Cotte, S.; Galipaud, J.; Pecquenard, B.; Le Cras, F. Thorough XPS analyses on overlithiated manganese spinel cycled around the 3V plateau. *Appl. Surf. Sci.* **2017**, *411*, 449–456. [CrossRef]
68. Dong, X.; Shen, W.; Gu, J.; Xiong, L.; Zhu, Y.; Li, A.H.; Shi, J. MnO_2-Embedded-in-Mesoporous-Carbon-Wall Structure for Use as Electrochemical Capacitors. *J. Phys. Chem. B* **2006**, *110*, 6015–6019. [CrossRef]
69. Singu, B.S.; Hong, S.E.; Yoon, K.R. Ultra-thin and ultra-long α-MnO_2 nanowires for pseudocapacitor material. *J. Solid State Electrochem.* **2017**, *21*, 3215–3220. [CrossRef]
70. Yang, Y.; Niu, H.; Qin, F.; Guo, Z.; Wang, J.; Ni, G.; Zuo, P.; Qu, S.; Shen, W. MnO_2 doped carbon nanosheets prepared from coal tar pitch for advanced asymmetric supercapacitor. *Electrochim. Acta* **2020**, *354*, 136667. [CrossRef]
71. Edison, T.N.J.I.; Atchudan, R.; Karthik, N.; Xiong, D.; Lee, Y.R. Direct electro-synthesis of MnO_2 nanoparticles over nickel foam from spent alkaline battery cathode and its supercapacitor performance. *J. Taiwan Inst. Chem. Eng.* **2019**, *97*, 414–423. [CrossRef]
72. Xue, C.; Hao, Y.; Luan, Q.; Wang, E.; Ma, X.; Hao, X. Porous manganese dioxide film built from arborization-like nanoclusters and its superior electrochemical supercapacitance with attractive cyclic stability. *Electrochim. Acta* **2019**, *296*, 94–101. [CrossRef]